

KCI 통합검색

통합검색 검색어를 입력해 주세요



HOME > 논문 검색 > 학술지 권호별 검색

논문 검색 | 원문 공개 논문 검색 | 학술지 권호별 검색 | 참고문헌 검색

권호목록

학술지 권호별 검색

2022

36권 7호

36권 6호

36권 5호

36권 4호

36권 3호

36권 2호

36권 1호

2021

2020

2019

2018

2017

2016

2015

2014

2013

2012

2011

2010

2009

2008

2007

2006

2005

2004

2003

2002

KCI 등재 SCIE SCOPUS

Journal of Mechanical Science and Technology (J. Mech. Sci. Tech.)

Journal of Mechanical Science and Technology (J. Mech. Sci. Tech.)

연구분야	공학 > 기계공학	ISSN	1738-494X
eISSN	1976-3824	창간 연도	1987 년
발행 간기	연12회	최근 발행정보	2022년 07월, 36(7)
언어	한국어 , 영어		

엑셀

번호	논문제목	저자명	페이지	피인용 횟수
1	Limiting the wind-induced deflection amplitude of an overhead conductor: establishment of multi-rigid-body model and optimization of structural parameters	Xin Hu	3205~3216	0
2	Modal parameter identification in atmospheric turbulence excitation flutter test based on Hilbert-Huang transform	Yang Li	3217~3226	0
3	Research on intelligent launching control of dual clutch transmissions based on adaptive neural fuzzy inference system	Guodong Zhao	3227~3237	0
4	Simulation of directional drilling by dynamic finite element method		3239~3250	0
5	The examination principle and the effect of vibration suppression of a rotor system equipped with a skew-mounted automatic ball balancer		3251~3262	0
6	Separation method of rolling bearing compound fault characteristics based on improved harmonic wavelet packet decomposition and fast ICA		3263~3276	0
7	Numerical studies on the dynamic characteristics of a wet multi-disc clutch during the disengaging process		3277~3289	0
8	Evaluation of failure criteria for composite plate under high-velocity impact		3291~3300	0
9	Kinematic analysis of particle movement in friction barrel-type tribocharger		3301~3312	0
10	Active structural acoustic control for radiated sound power reduction of enclosure with vent holes based on radiation modes		3313~3327	0
11	Mechanical characteristics and experimental research of a flexible rope-sheave hoisting mechanism		3329~3339	0
12	Fatigue life prediction model of Ti-6Al-4V alloy forgings based on forging process parameters		3341~3352	0
13	Variations of stress and deformation in the straightening process of turnout base plate		3353~3360	0
14	A simulation of the comminution process of homogenized lithium-ion battery models		3361~3372	0
15	A comparative study of mechanical behavior of ABS material based on UVC sterilization for medical usage		3373~3385	0
16	The experimental and numerical investigation on thermal responses of passive thermal protected batteries in different packs from low to high discharge rates		3387~3398	0
17	Prediction of operating reliability of multi-body mechanism in micro-switches considering parameter distribution and wear of parts		3399~3407	0
18	Ductile tearing criteria and failure probability estimation of hydrided Zircaloy-4 cladding under axial loads		3409~3417	0

번호	논문제목	저자명	페이지	피인용 횟수
19	High-temperature tensile behavior of diffusion-welded hastelloy X		3419~3428	0
20	Analysis of EL images on Si solar module under thermal cycling		3429~3436	0
21	Effect of rotating, non-axisymmetric cavitator on supercavity size		3437~3447	0
22	Experimental investigation of surface roughness effect on a free-flight sphere in a Ludwig tube		3449~3456	0
23	Effect of the opening of a butterfly valve on the dynamic evolution of cavitation		3457~3467	0
24	A fluid-structure interaction analysis of design factor of subsurface irrigation PC dripper		3469~3475	0
25	Aggregation behavior analysis of hydrate particles in the bend pipe based on the population balance model		3477~3486	0
26	Effect of blade tip pattern on blade load and vibration characteristics of a twin-stage axial flow fan		3487~3500	0
27	Experimental investigation of low-frequency instabilities of dual-swirl pressure-atomization spray flames		3501~3508	0
28	Bi-directional evolutionary 3D topology optimization with a deep neural network		3509~3519	0
29	Numerical study of coupling damage between contact fatigue and sliding wear		3521~3533	0
30	Multi-objective optimization of cycloidal gear based on segmental modification of pressure angle		3535~3545	0
31	Multi-objective variable parameter optimization algorithm for spiral bevel gear tooth surface considering meshing efficiency and contact performance		3547~3559	0
32	Particle generation to minimize the computing time of the discrete element method for particle packing simulation		3561~3571	0
33	Time-evolution of electrical resistance-strain hysteresis curve of embroidered stretch sensors and their application in reliable human motion tracking		3573~3584	0
34	Lightweight design of hinge beam based on Kriging agent model		3585~3595	0
35	Numerical analysis of elastohydrodynamic lubrication characteristics of the spatial cam mechanism in the air splicer		3597~3607	0
36	A helix slope deviation compensation model for milling small modulus copper electrode gears		3609~3618	0
37	Thermal effect of high-velocity particle impingements on coating quality in cold gas dynamic spray operations		3619~3629	0
38	Experimental study on ultrasonic-assisted grinding of micro-structured surface on silicon carbide using small diameter grinding wheel		3631~3642	0
39	Tool life evaluation of CFRP drilling with three kinds of drill		3643~3651	0
40	Motion blur processing method for visual SLAM system based on local residual blur discrimination network		3653~3666	0
41	Ridge-following control for agricultural tractors using deep learning and stereo camera		3667~3675	0
42	Vibration isolation control performance for an innovative 3-DOF parallel stabilization platform		3677~3689	0
43	Boiling heat transfer-based temperature rise characteristics of automotive permanent magnet synchronous motors at peak operating conditions		3691~3699	0
44	Numerical analysis of thermal dynamics and mixing performance in the blade-type static mixers		3701~3716	0
45	Effect of steering wheel heating system on hand thermal sensation		3717~3725	0
46	Thermal management modeling for cylindrical lithium-ion battery packs considering safety and lifespan		3727~3733	0
47	Operating characteristics of a flat evaporator loop heat pipe having a flexible heat transport path		3735~3751	0
48	Theoretical modelling and simulation analysis of the thermal performance of a steel-basalt fiber polymer concrete machine tool joint surface		3753~3765	0
49	Preload control of the increased outflow of a dual pulsatile extracorporeal membrane oxygenator		3767~3772	0
50	Erratum : Research on feature enhancement method of weak fault signal of rotating machinery based on adaptive stochastic resonance	Kangping Gao	3773~3774	0
51	Erratum : A novel investigation in the performance, combustion and emission characteristics of variable compression ratio engine using bio-diesel blends	R. Tamilselvan	3775~3775	0

번호	논문제목	저자명	페이지	피인용 횟수
52	Erratum : Numerical study on the shock vector control performance in a de Laval nozzle with single or dual injection ports		3777~3777	0

Original Article

DOI 10.1007/s12206-022-0538-3

Keywords:

- Cohesive zone model
- Composite lattice structure
- Interlaminar fracture toughness
- Crack propagation

Correspondence to:

Kwang-Bok Shin
shin955@hanbat.ac.kr

Citation:

Im, J.-M., Shin, K.-B. (2022). Study on the prediction method of onset and propagation of damage of unit composite lattice structure. *Journal of Mechanical Science and Technology* 36 (6) (2022) 3081~3088. <http://doi.org/10.1007/s12206-022-0538-3>

Received November 17th, 2021

Revised February 2nd, 2022

Accepted February 12th, 2022

† Recommended by Editor
Hyun-Gyu Kim

Study on the prediction method of onset and propagation of damage of unit composite lattice structure

Jae-Moon Im¹ and Kwang-Bok Shin²

¹Graduate School of Mechanical Engineering, Hanbat National University, Daejeon 34158, Korea, ²Department of Mechanical Engineering, Hanbat National University, Daejeon 34158, Korea

Abstract The progressive failure behavior of a unit composite lattice structure under compressive load was predicted using cohesive zone model (CZM). Mode I, II and mixed mode I/II interlaminar fracture toughness tests were conducted to obtain a set of cohesive zone parameters. To predict failure behavior through numerical analysis, a FEM was generated by considering the three problems of composite lattice structure: differences in the fiber volume fraction, discontinuity in mechanical properties, and generation of wedge-shaped resin rich parts. To select the position of cohesive elements, first numerical analysis was performed, and cohesive elements were applied to the layer with the highest failure index of quadratic nominal stress criterion. The results of numerical analysis with cohesive element were well matched with the test result. These results showed that CZM based numerical analysis method is an effective way to predict and evaluate the onset and growth of progressive failure of unit composite lattice structure.

1. Introduction

Composite materials are well known for being lightweight, with higher specific stiffness and specific strength than metallic materials, and are widely used to improve structural performance extremely in the aerospace, defense, and transportation industries. In particular, lattice structures, which are used to manufacture rockets, missiles, and projectiles in the aerospace and military fields, need reduced weight to improve performance. For this reason, lattice structures are now mainly fabricated with composites to reduce weight in high-performance guided missiles, space launch vehicles, aircraft fuselages, etc., where the weight of the structure has a significant influence on performance.

The composite lattice structure is comprised of repeating structural units having the minimum cross-section area needed to support the required loads. A typical example of a composite lattice structure is the interstage of the Proton-M rocket, which is a composite lattice structure manufactured by the filament winding method [1-3]. Fig. 1 shows the interstage of the Proton-M rocket.

Many studies have been conducted on composite lattice structures. Vasiliev established a design theory for composite lattice structures based on beam theory, and this theory aims to minimize the mass of the lattice structure through Eq. (1) [4].

$$M = 2\pi RL'H \left(2\rho_h \frac{\delta_h}{a_h} + \rho_c \frac{\delta_c}{a_c} \right) \quad (1)$$

Belardo conducted a study on the design of a re-entry vehicle using composite lattice structure [5], while Krishan designed a composite lattice structure tank inside the space launch vehicle [6]. Querin studied the application of composite lattice structure to aircraft fuselage using a topology optimization method [7], and Kanou evaluated the structural performance of a cylindri-



Fig. 1. Interstage of Proton-M rocket.

cal composite lattice structure using a numerical method [8]. But while many studies have been conducted on the composite lattice structure, detailed studies on their failure behavior are lacking.

Composite lattice structures are commonly fabricated using the filament winding method, or automated fiber placed (AFP) method. Given the characteristics of the fiber reinforced composite, fiber intersections occur, which causes three structural problems. The first is the difference in the number of stacks; at the fiber intersection, twice as many fibers are stacked compared to a non-intersection, causing a difference in the fiber volume fraction. The second is the discontinuity of mechanical properties at the fiber intersection, which also occurs because of the difference in the number of stacks at the fiber intersection. The third is the generation of resin-rich parts. Because of the difference in the number of stacks, wedge-shaped resin-rich parts are generated at the boundaries of the fiber intersections. These problems can weaken the structural performance of the composite lattice structure, and consequently it is necessary to evaluate how these factors affect structural performance.

In this study, a finite element model was generated to consider the three problems, and to evaluate the exact structural performance of a composite lattice structure manufactured by the filament winding method through numerical analysis. In addition, CZM was applied to predict the progressive failure behavior of composite lattice structures. To obtain a set of cohesive parameters for the cohesive material, tests were performed using double cantilever beam (DCB), end notched flexure (ENF), and mixed mode bending (MMB) specimens. All specimens had the same materials with a composite lattice structure and were manufactured by the filament winding method. The performance was evaluated on a unit composite lattice structure of the whole composite lattice structure. Then, to verify the reliability of the proposed simulation procedure, the results of the unit composite lattice structure test were compared with the load-displacement curve obtained from numerical analysis.

2. Interlaminar fracture toughness test

2.1 Specimen

The specimens used to evaluate interlaminar fracture toughness were manufactured using the same materials and same

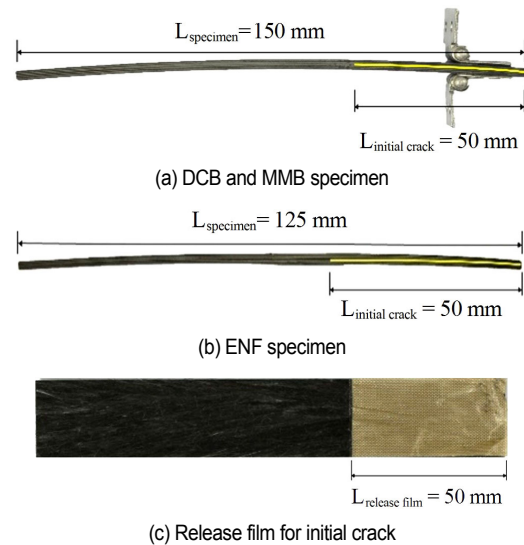


Fig. 2. Mode test specimens.

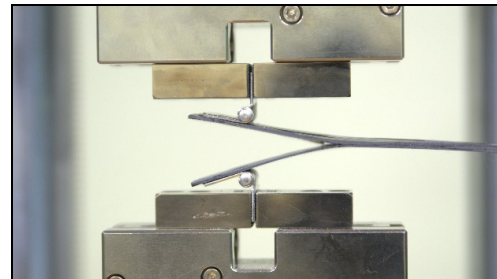


Fig. 3. Mode I test.

fabrication method as the composite lattice structure. These were manufactured using T700 grade carbon fiber and the filament winding method.

The interlaminar fracture toughness tests were conducted with double cantilever beam (DCB), end notched flexure (ENF), and mixed mode bending (MMB). The DCB specimens for mode I test and MMB specimens for mixed mode I/II test were 150 mm long and 25 mm wide, and the ENF specimens for mode II test were 125 mm long and 25 mm wide. The initial crack of 50 mm was created using release film. Fig. 2 shows DCB, MMB, ENF specimens, and release film for initial crack which is placed in middle layer.

2.2 Fracture toughness test

The mode I test was performed using DCB specimens based on ASTM D5528 [9]. Mode II and mixed mode I/II tests were conducted using ENF and MMB specimens in accordance with ASTM D6671 [10]. Figs. 3-5 show mode I, mode II, and mixed mode I/II tests, respectively. A load was imposed with a controlled displacement of 1 mm/min for the tests. The mixed mode I/II ratios were set at 0.25, 0.5, and 0.75; and the lever length was changed to set the position of the load point. Mode I tests were conducted with opening fracture mode as shown in



Fig. 4. Mode II test.

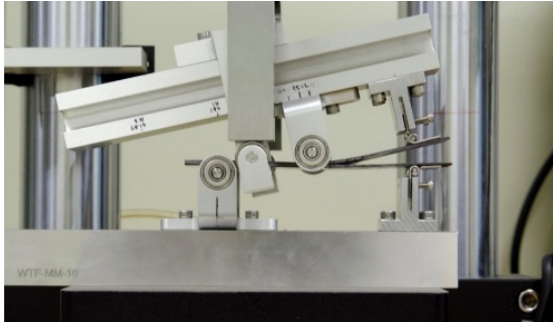


Fig. 5. Mixed mode I/II test.

Fig. 3. Mode I interlaminar fracture toughness was calculated with Eq. (2), using modified beam theory.

$$G_{Ic} = \frac{3P\delta}{2ba} \quad (2)$$

Mode II interlaminar fracture toughness was evaluated using ENF specimen as shown in Fig. 4. The mode II interlaminar fracture toughness was calculated by Eq. (3) using maximum load and corresponding displacement.

$$G_{IIc} = \frac{9a^2P\delta}{2b(2L^3 + 3a^3)} \quad (3)$$

MMB specimen is the most widely used for evaluating interlaminar fracture toughness of mixed mode I/II as shown in Fig. 5. The advantage of using the MMB specimen is being able to change the mixed mode ratio, from pure mode I to pure Mode II. In this study, the mixed mode I/II interlaminar fracture toughness was obtained by adding the results of Eqs. (4) and (5) [10].

$$G_I = \frac{3P^2(3c-L)^2}{4b^2h^3L^2E_{II}} \left[a^2 + \frac{2a}{\lambda} + \frac{1}{\lambda^2} + \frac{h^2E_{II}}{10G_{I3}} \right] \quad (4)$$

$$G_{II} = \frac{9P^2(c+L)^2}{16b^2h^3L^2E_{II}} \left[a^2 + \frac{0.2h^2E_{II}}{G_{I3}} \right] \quad (5)$$

The interlaminar fracture toughness tests were conducted

Table 1. Test results of interlaminar fracture toughness.

G_{II}/G_I (Mixed mode ratio)	0.00	0.25	0.50	0.75	1.00
G_c (J/m ²)	264.57	462.01	809.07	1068.43	3689.3



Fig. 6. Test equipment (Instron 5848).

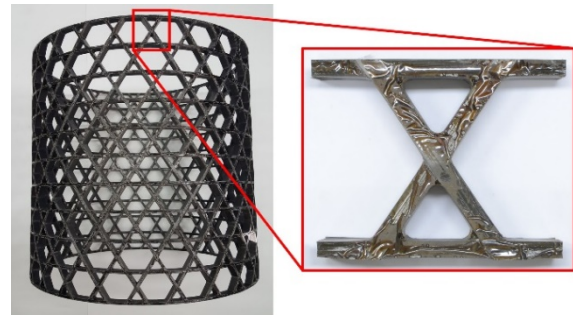


Fig. 7. Unit composite lattice structure specimens.

using an Instron 5848 with 10 kN capacity, as shown in Fig. 6. Table 1 shows the test results of interlaminar fracture toughness. In mixed mode I/II test results, the more it has high ratio of mode II, the higher interlaminar fracture toughness occurs because mode II interlaminar fracture toughness is much higher than mode I interlaminar fracture toughness.

3. Unit composite lattice structure test

To evaluate the structural performance of unit composite lattice structure, a compressive test was conducted. The composite lattice structure used in this study was cylindrical and had the same dimensions as those shown in Table 2. The unit composite lattice structure specimens were taken from whole composite lattice structure as shown in Fig. 7.

The compressive test of unit composite lattice structure was conducted using Instron 4484 with 150 kN capacity, as shown in Fig. 8. And the anti-buckling fixture for compressive test was manufactured by referring to ASTM D6641 [11]. Each rod of the fixture was placed on either side to maintain the alignment. A load was imposed with a controlled displacement of 1 mm/min for the tests. Fig. 9 shows compressive test of unit

Table 2. Dimensions of composite lattice structure.

	Value
Mass (kg)	10.59
No. of helical ribs	24
No. of hoop ribs	11
Width of eibs (mm)	6.7
Thickness of eib (mm)	16.5
Helical angle	32°
Length of structure (mm)	617.87



Fig. 8. Test equipment (Instron 4484).

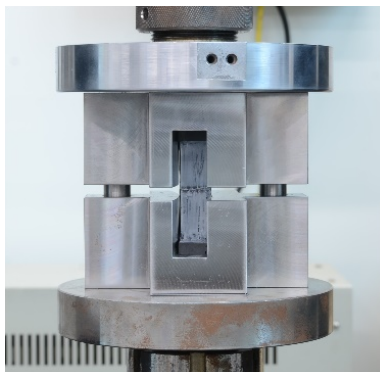


Fig. 9. Compressive test of unit composite lattice structure.

composite lattice structure.

The results of compressive test of unit composite lattice structure are shown in Fig. 10. Unit composite lattice structure specimens failed about 74598 N of load and 1.03 mm of displacement. And delamination failure mode occurred at the boundary of helical rib-hoop rib fiber intersection, as shown in Fig. 11. The failure at the boundary of helical rib-hoop rib fiber intersection was caused by stress concentration due to the wedge-shaped resin rich part and shape of the structure. And

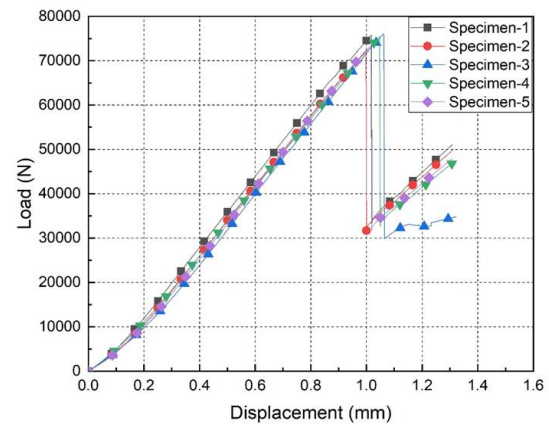


Fig. 10. Load-displacement curve of compressive test.

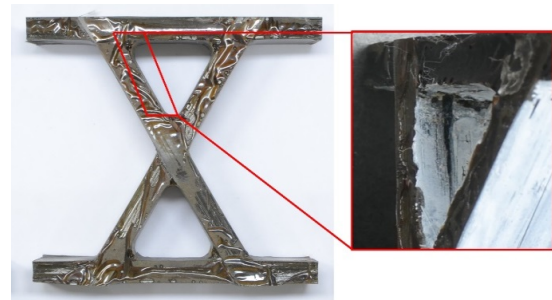


Fig. 11. Delamination failure mode.

the crack grew along the helical rib following the load direction.

4. Analysis of unit composite lattice structure

A numerical analysis for evaluating structural performance of unit composite lattice structure was conducted using ABAQUS V.6.13. Finite element model employed for the evaluation was generated by considering the fiber intersections and the resin rich parts. A cross section of the fiber intersection of an actual structure is shown in Fig. 12.

To replicate all the layers of the actual structure identically, 50 layers and 25 layers were applied at fiber intersections and non-intersections, respectively. The finite element model was generated to consider the winding pattern of the actual structure. The resin-rich part shown in Fig. 12 was applied to finite element model with the same size of real resin-rich part. In Fig. 13, the red triangle elements are wedge-shaped resin-rich parts. These were generated by following fiber winding stack.

First, numerical analysis without cohesive element was conducted to select the position to apply the cohesive elements. The load and boundary conditions of the numerical analysis were selected based on the anti-buckling fixture in the compressive test of the unit composite lattice structure. Fig. 14 shows the load and boundary conditions of structural analysis. In addition, mechanical properties were classified and applied

Table 3. Mechanical properties of composite lattice structure.

Mechanical properties		Fiber volume fraction	
		0.7	0.3
Elastic modulus (GPa)	E_{11}	134.26	74.82
	E_{22}	8.08	6.64
	E_{33}	8.08	6.64
Tensile strength (MPa)	S_{11}	2480.80	1512.05
	S_{22}	44.16	60.30
	S_{33}	44.16	60.30
Compressive strength (MPa)	C_{11}	1170.67	398.25
	C_{22}	128.98	85.74
	C_{33}	128.98	85.74
Shear modulus (GPa)	G_{12}	5.33	2.28
	G_{13}	5.33	2.28
	G_{23}	2.74	1.17
Shear strength (MPa)	τ_{12}	82.60	33.61
Poisson ratio	ν_{12}	0.33	0.33
	ν_{13}	0.33	0.33
	ν_{23}	0.45	0.45



Fig. 12. Cross-section of fiber intersection part.

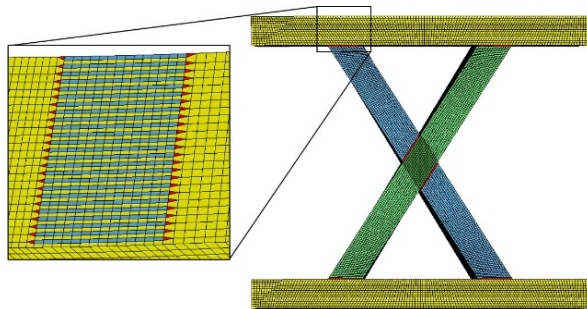


Fig. 13. Finite element model of unit composite lattice structure.

by considering the fiber volume fraction of the fiber intersections and non-intersections, as shown in Fig. 15.

The mechanical properties at a fiber volume fraction of 0.7 were obtained in a previous study, and mechanical properties at a fiber volume fraction of 0.3 were calculated using the rule of mixture in Eqs. (6)-(8), as shown in Table 3 [12-14].

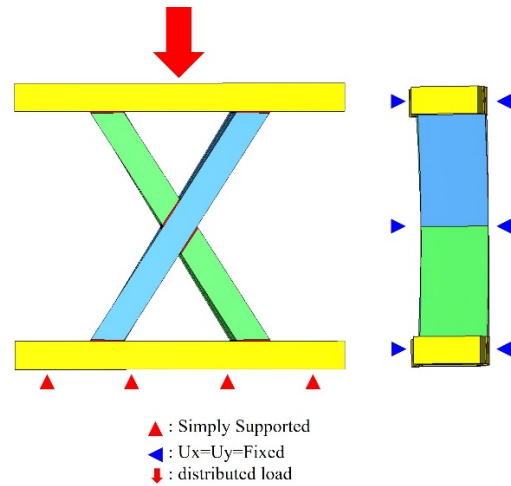


Fig. 14. Load and boundary condition.

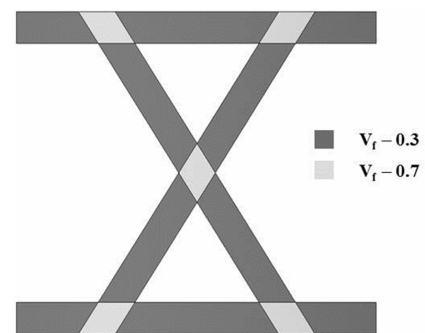


Fig. 15. Fiber volume fraction of composite lattice structure.

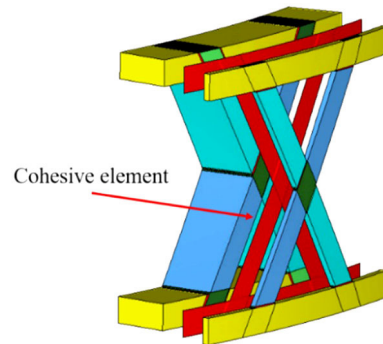


Fig. 16. Position of cohesive element.

$$E_L = v_f E_f + v_m E_m \quad (6)$$

$$E_T = \frac{E_f E_m}{v_f E_m + v_m E_f} \quad (7)$$

$$\sigma_{cl} = \sigma_m (1 - V_f) + \sigma_f V_f \quad (8)$$

As a result of the structural analysis, the highest failure index of quadratic nominal stress criterion was in the outer diameter direction, so the cohesive elements were applied to the layer with highest failure index of quadratic nominal stress criterion as shown in Fig. 16.

The cohesive elements were applied with a solid element with zero thickness using COH3D8 provided by ABAQUS. The finite element model had 249564 nodes and 221100 elements.

In the CZM, the onset of damage is determined by stress states. Cui showed the importance of the interactions between interlaminar stress components when cracks produced. The load which is applied to unit composite lattice structure occurred as a mixed mode load, so considering interactions between interlaminar stress components is important to predict damage onset. The quadratic nominal stress criterion shown in Eq. (9), which was proposed by Cui, was used to predict the onset of damage of unit composite lattice structure [14].

$$\left(\frac{\sigma_n}{N_{\max}}\right)^2 + \left(\frac{\sigma_s}{T_{\max}}\right)^2 + \left(\frac{\sigma_t}{S_{\max}}\right)^2 = 1 \quad (9)$$

The power law criterion is the most widely used for the prediction of damage growth under mixed mode loading, expressed as Eq. (10). It provides conservative results of damage growth in epoxy composites. However, it can derive inaccurate results over a various range of mixed mode ratios [15].

$$\left(\frac{G_I}{G_{IC}}\right)^\alpha + \left(\frac{G_{II}}{G_{IIC}}\right)^\alpha = 1 \quad (10)$$

Thus, the B-K criterion suggested by Benzeggagh and Kenane was used to predict damage growth in this study [16]. This criterion is composed of the fracture toughness of mode I and mode II, and a parameter η obtained from the mixed mode I/II test, as shown in Eq. (11):

$$G_{IC} + (G_{IIC} - G_{IC}) \left(\frac{G_{II}}{G_I}\right)^\eta = G_C \quad (11)$$

It was found that η is 4.40, calculating an equation obtained from least square regression curve fit of interlaminar fracture toughness test data.

A bilinear traction-separation law, which can be easily applied to CZM, was selected and applied as shown in Fig. 17. Cohesive stiffness was derived through Eqs. (12) and (13) as suggested by Dihel [17]. The cohesive parameters applied to the prediction are shown in Table 4. Through earlier study, δ_f was chosen as element size of 0.05 times [18, 19]. The orientation of cohesive elements was based on direction of cohesive zone parameters.

$$G_C = \frac{1}{2} \tau_{ult} \delta_f \quad (12)$$

$$K = \frac{2G_C}{\delta_{ratio} \delta_f^2} \quad (13)$$

Progressive failure analysis was conducted using the finite element model with the cohesive elements in Fig. 16. The load

Table 4. Cohesive parameters for interlaminar material.

Parameters		Value
Cohesive stiffness (N/mm ²)	K_I	9525
	K_{II}	59340
	K_{III}	59340
Cohesive strength (MPa)	$\tau_{ult,1}$	5.95
	$\tau_{ult,2}$	82.97
	$\tau_{ult,3}$	82.97

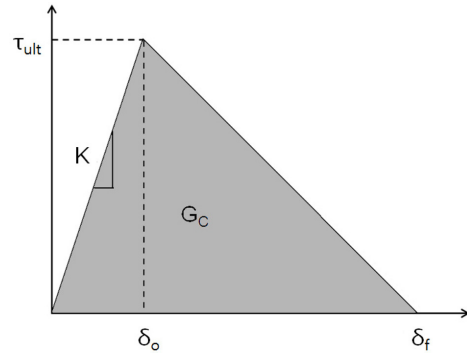


Fig. 17. Bilinear traction-separation law diagram.

and boundary conditions from Fig. 14 were applied and the analysis was performed using ABAQUS V.6.13.

First, the damage area of cohesive zone occurred at inter-sections. As the load increased, the cracks grew along the helical ribs. Finally, delamination generated at the boundary of helical-hoop ribs and helical-helical ribs. Fig. 18 shows the onset and growth of delamination of unit composite lattice structure. The delamination areas were distributed symmetrically with fiber direction because of its stacking sequence. Also, when compared with the position of the fracture in the test, the position was the same as confirmed in Fig. 11.

In the test, failure occurred at a load of 74598 N and a displacement of 1.03 mm, and in the analysis, failure occurred at a load of 78862 N and a displacement of 1.00 mm. The result of the progressive failure analysis is shown in Fig. 19. It was confirmed that the error in load between test and analysis was 5.72 %, and the error in displacement was 2.82 %.

The onset of fracture occurred at the boundary of helical rib-hoop rib fiber intersection, because at the fiber intersection of the helical ribs, each helical rib, fiber direction and load transfer direction coincide and the energy release rate ratio of mode II is higher than mode I, whereas the fiber intersection of the helical rib and hoop rib has high portion of ratio of mode I, which has relatively low critical energy release rate. While in helical rib-hoop rib fiber intersection, the helical ribs support the load alone and the hoop ribs support maintaining its shape. So the helical rib-hoop rib fiber intersection failed earlier than helical ribs intersections.

The comparison of the test and analysis results and failure mode confirmed that the method of evaluating progressive failure by applying CZM can be accurately used to predict onset and

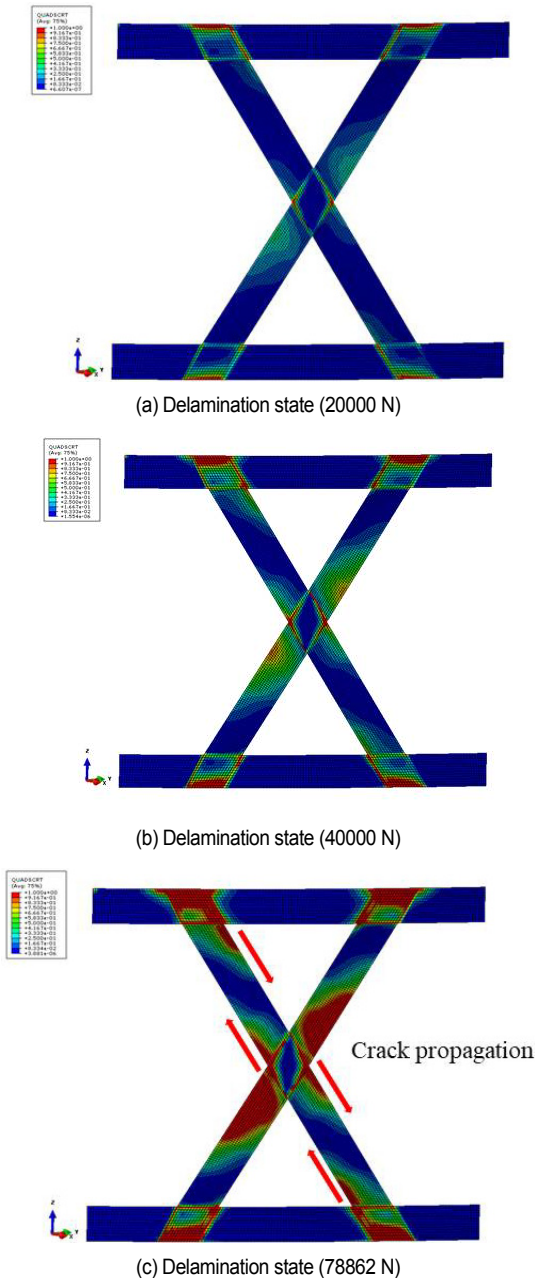


Fig. 18. Result of progressive failure analysis.

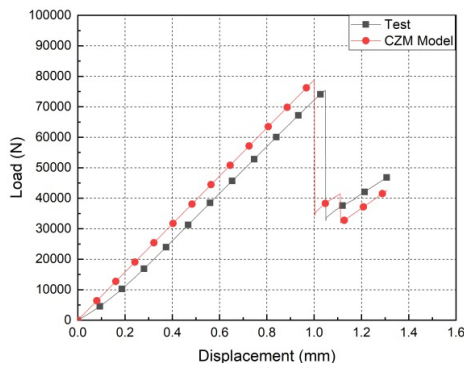


Fig. 19. Load-displacement curve of test and analysis.

propagation of damage of the unit composite lattice structure.

5. Conclusions

Composite lattice structures can have failure problems caused by differences in fiber volume fraction, discontinuity in mechanical properties, and the generation of wedge-shaped resin-rich parts. These three problems can result in the fracture of the composite lattice structure through crack growth after interlaminar fracture onset. To predict the accurate structural performance of a composite lattice structure, it is therefore necessary to consider these modes of progressive failure.

In this study, a progressive failure analysis was conducted using CZM to predict the structural performance of a unit composite lattice structure. Analysis was performed using a unit composite lattice structure, and cohesive elements were applied inside the structure. Reliability was verified by comparing the results of the progressive failure analysis with test results, and the conclusions are as follows:

- 1) To predict the progressive failure of a unit composite lattice structure, mode tests were conducted and cohesive parameters were obtained.
- 2) A finite element model was generated by considering the three problems of composite lattice structures, which are differences in fiber volume fraction, discontinuity in mechanical properties, and the generation of wedge-shaped resin-rich parts.
- 3) Numerical analysis was performed to select the position to apply the cohesive element, and the cohesive element was applied to the layer with the highest failure index of quadratic nominal stress criterion.
- 4) As a result of the progressive failure analysis of the unit composite lattice structure, an error of up to 6 % was confirmed with the test. The results showed that the method using CZM was effective for predicting and evaluating the onset and growth of fracture, and the structural performance of unit composite lattice structure.

Nomenclature

a	: Crack length
a_c	: Distance between hoop ribs
a_h	: Distance between helical ribs
b	: Width of the specimen
c	: Lever length
E_f	: Fiber modulus
E_L	: Longitudinal direction modulus
E_m	: Matrix modulus
E_T	: Transverse direction modulus
G_I	: Mode I energy release rate
G_{II}	: Mode II energy release rate
G_{IC}	: Critical energy release rate for mode I
G_{IIC}	: Critical energy release rate for mode II
G_C	: Sum of G_{IC} and G_{IIC}
G_T	: Total energy release rate
H	: Thickness of lattice structure

h	: Half-thickness of specimen
K	: Cohesive stiffness
L	: Half-span of specimen
L'	: Length of lattice structure
M	: Mass of lattice structure
N_{max}	: Maximum interlaminar normal tensile strength
P	: Load
R	: Radius of lattice structure
S_{max}	: Maximum interlaminar sliding shear strength
T_{max}	: Maximum interlaminar scissoring shear strength
δ	: Displacement
δ_c	: Thickness of hoop rib
δ_f	: Cohesive ductility
δ_h	: Thickness of helical rib
λ	: Crack length correction parameter
ν_f	: Fiber Poisson ratio
ν_m	: Matrix Poisson ratio
ρ_c	: Density of hoop rib
ρ_h	: Density of helical rib
σ_n	: Nominal stress in the pure normal direction
σ_s	: Nominal stress in the first shear direction
σ_t	: Nominal stress in the second shear direction
$\tau_i (i = 1, 2, 3)$: Interfacial normal or shear tractions for pure mode I
τ_{ult}	: Ultimate stress

References

- [1] V. V. Vasiliev and A. F. Rasin, Anisogrid composite lattice structures for spacecraft and aircraft applications, *Composite Structures*, 76 (2006) 182-189.
- [2] V. V. Vasiliev, V. A. Barynin and A. F. Rasin, Anisogrid lattice structures-survey of development and applications, *Composite Structures*, 54 (2011) 361-370.
- [3] V. V. Vasiliev, V. A. Barynin and A. F. Rasin, Anisogrid composite lattice structures-development and aerospace applications, *Composite Structures*, 94 (2012) 1117-1127.
- [4] V. A. Barynin, V. A. Bunakov, A. F. Rasin and V. V. Vasiliev, Aerospace composite lattice structure, *Proc. of ICCM*, Paris, France (2009).
- [5] M. Belardo, N. Paletta and U. Mercurio, Conceptual design of the composite sandwich fuselage of a re-entry vehicle, *Materiawissenschaft und Werkstofftechnik*, 46 (4-5) (2015) 420-430.
- [6] P. K. Krishan and P. Muruganatham, Design and analysis of a typical inter-tank structure of a launch vehicle using integrally stiffened construction, *International J. of Research in Engineering and Technology*, 1 (1) (2013) 21-34.
- [7] O. M. Querin et al., *Topology and Parametric Optimization of a Lattice Composite Fuselage Structure*, Altair University, Retrieved April 13 (2021) https://altairuniversity.com/wp-content/uploads/2014/04/Topology_and_Parametric_Optimization-of-a-Lattice_Composite_Fuselage_Structure_as_published.pdf (2014).
- [8] H. Kanou, S. M. Nabavi and J. E. Jam, Numerical modeling of stresses and buckling loads of isogrid lattice composite structure cylinders, *International of Engineering, Science and Technology*, 5 (1) (2013) 42-54.
- [9] ASTM D5528, *Standard Test Method for Mode I Interlaminar Fracture Toughness of Unidirectional Fiber-reinforced Polymer Matrix Composites*, ASTM International (2001).
- [10] ASTM D6671, *Standard Test Method for Mixed Mode I-Mode II Interlaminar Fracture Toughness of Unidirectional Fiber Reinforced Polymer Matrix Composites*, ASTM International (2006).
- [11] ASTM D6641, *Standard Test Method for Compressive Properties of Polymer Matrix Composite Materials Using a Combined Loading Compression (CLC) Test Fixture*, ASTM International (2009).
- [12] R. F. Gibson, *Principles of Composite Material Mechanics*, CRC Press, Florida, USA (2011).
- [13] W. D. Callister, Jr. and D. G. Rethwisch, *Fundamentals of Materials Science and Engineering: An Integrated Approach*, 2nd ed., Wiley, Hoboken, USA (2004) 592.
- [14] D. Hull and T. W. Clyne, *An Introduction to Composite Materials*, 2nd ed, Cambridge University Press, New York, USA (1996) 177-179.
- [15] W. Cui, M. Wisnom and M. Jones, A comparison of failure criteria to predict delamination of unidirectional glass/epoxy specimens waisted through the thickness, *Composites*, 23 (3) (1992) 158-166.
- [16] P. P. Camanho, C. G. Davila and M. F. de Moura, Numerical simulation of mixed-mode progressive delamination in composite materials, *J. of Composite Materials*, 37 (16) (2003) 1415-1438.
- [17] M. Kenane and M. L. Benzeggagh, Mixed-mode delamination fracture toughness of unidirectional glass/epoxy composites under fatigue loading, *Composites Science and Technology*, 57 (5) (1997) 597-605.
- [18] T. Diehl, On using a penalty-based cohesive-zone finite element approach, part I: elastic solution benchmarks, *International J. of Adhesion and Adhesives*, 28 (4) (2008) 237-255.
- [19] J. M. Im, S. G. Kang, K. B. Shin and T. K. Hwang, Prediction of onset and propagation of damage of in the adhesive joining of a dome-separated composite pressure vessel including temperature effects, *International J. of Precision Engineering and Manufacture*, 18 (12) (2017) 1795-1804.



Jae-Moon Im is a Ph.D. candidate in Mechanical Engineering, Hanbat National University, Daejeon, Rep. of Korea. His research interest is in composite materials and structures.



Kwang-Bok Shin is a Professor of Mechanical Engineering, Hanbat National University, Daejeon, Rep. of Korea. His research interest is in composite material, composite structures and CAE.